

Flat bands and extreme pseudomagnetic fields in monolayer graphene by topography strain engineering

Xiaoyi Yuan  and Shuze Zhu *

Center for X-Mechanics, Key Laboratory of Soft Machines and Smart Devices of Zhejiang Province, Department of Engineering Mechanics, Institute of Applied Mechanics, Zhejiang University, Hangzhou 310000, China



(Received 20 January 2024; revised 26 April 2024; accepted 21 May 2024; published 7 June 2024)

Realizing flat bands via strong pseudomagnetic fields has recently inspired new opportunities for studying strong correlations in monolayer graphene, where a feasible idea is to utilize substrate topography to create strained graphene superlattices. Nevertheless, the effect from topography-induced strain relaxation on these isolated flat bands in monolayer graphene is unknown, posing challenges for rational design on flat bands and pseudomagnetic fields by strain engineering. In this work, we reveal analytical displacement fields due to strain relaxation in monolayer graphene conforming to substrate topography, allowing quantum mechanical design on flat band structures and strong pseudomagnetic fields in monolayer graphene with strain energy minimized. We find that the strong pseudomagnetic fields as well as flat band structures in monolayer graphene are highly sensitive to strain relaxation and substrate topography. The tunability of flat bands in monolayer graphene coupled to several topography designs is demonstrated. Our results contribute to the understanding of flat bands and strong pseudomagnetic fields in monolayer graphene enabled by topography strain engineering.

DOI: [10.1103/PhysRevB.109.245408](https://doi.org/10.1103/PhysRevB.109.245408)

I. INTRODUCTION

Recent years have witnessed considerable efforts to induce band flattening in graphene systems, given that flat bands facilitate the emergence of strongly correlated electronic phases and topological properties [1–10]. A well-known method is applying interlayer rotation between graphene layers [1,11–14], where a flat, narrow band appears near the Fermi level when the interlayer rotation angles approach several particular angles (also known as magic angles). The key challenge is to provide fine control over moiré patterns due to interlayer twisting, which may not be a straightforward task [15]. On the other hand, emerging evidence of flat bands and correlated states in buckled monolayer graphene [2,16–18] has inspired opportunities of realizing narrow bands towards strong correlations in monolayer graphene [19], even with the advantages of larger interaction-induced gaps, smaller quasiparticle dispersion, and enhanced tunability compared to the moiré system [19]. Importantly, the band flattening in monolayer graphene correlates with periodic arrays of strain-induced pseudomagnetic fields [2,16,20]. With such understanding, the concept of strain engineering [21–28] in monolayer graphene for tuning isolated flat bands has attracted growing attention [19], where a feasible idea is to utilize profiled surfaces to host strained graphene superlattices [21]. Strain relaxation is essential for strain engineering. Earlier tight-binding studies have shown that strain relaxation strongly affects pseudomagnetic fields in the triaxially stretched graphene hexagon [21,29].

Recently, monolayer graphene conforming to profiled substrate topography [20,30] has been proposed to controllably realize flat bands that resemble those found in buckled monolayer graphene [2,16–18]. Nevertheless, the effect of topography-induced strain relaxation on these isolated flat bands has remained unknown. In most available tight-binding calculations for these flat bands of monolayer graphene [2,16–18,20], the strain-coupled hopping energies are extracted from the presumed profile of periodic pseudomagnetic fields so that how the strain relaxation affects flat bands and associated pseudomagnetic fields remains elusive. In a recent study employing substrate engineering and optical control to tune the flat bands [30], the in-plane relaxation of graphene conforming to the substrate topography is discussed using an indeterminate dimensionless fitting parameter, unable to quantify the role of strain relaxation for different substrate topographies. Because the relaxed displacement fields coupled to substrate topography are not available [2,16], the fundamental roles of strain relaxation towards flat bands in strained monolayer graphene have not been addressed in existing quantum mechanical calculations [17,18,20,30], posing challenges for rational design on flat bands and associated pseudomagnetic fields in monolayer graphene.

To address the above issues, this work reveals analytical displacement fields due to strain relaxation in monolayer graphene conforming to substrate topography, allowing quantum mechanical design on electronic states directly from substrate topography with relaxation fully considered. Although strain relaxation is often treated as a higher order correction [30], our quantified calculations show that strain relaxation can significantly affect band structure in monolayer graphene containing flat bands, as well as the emergence of strong pseudomagnetic fields. We reveal several substrate

*Corresponding author: shuzezhu@zju.edu.cn

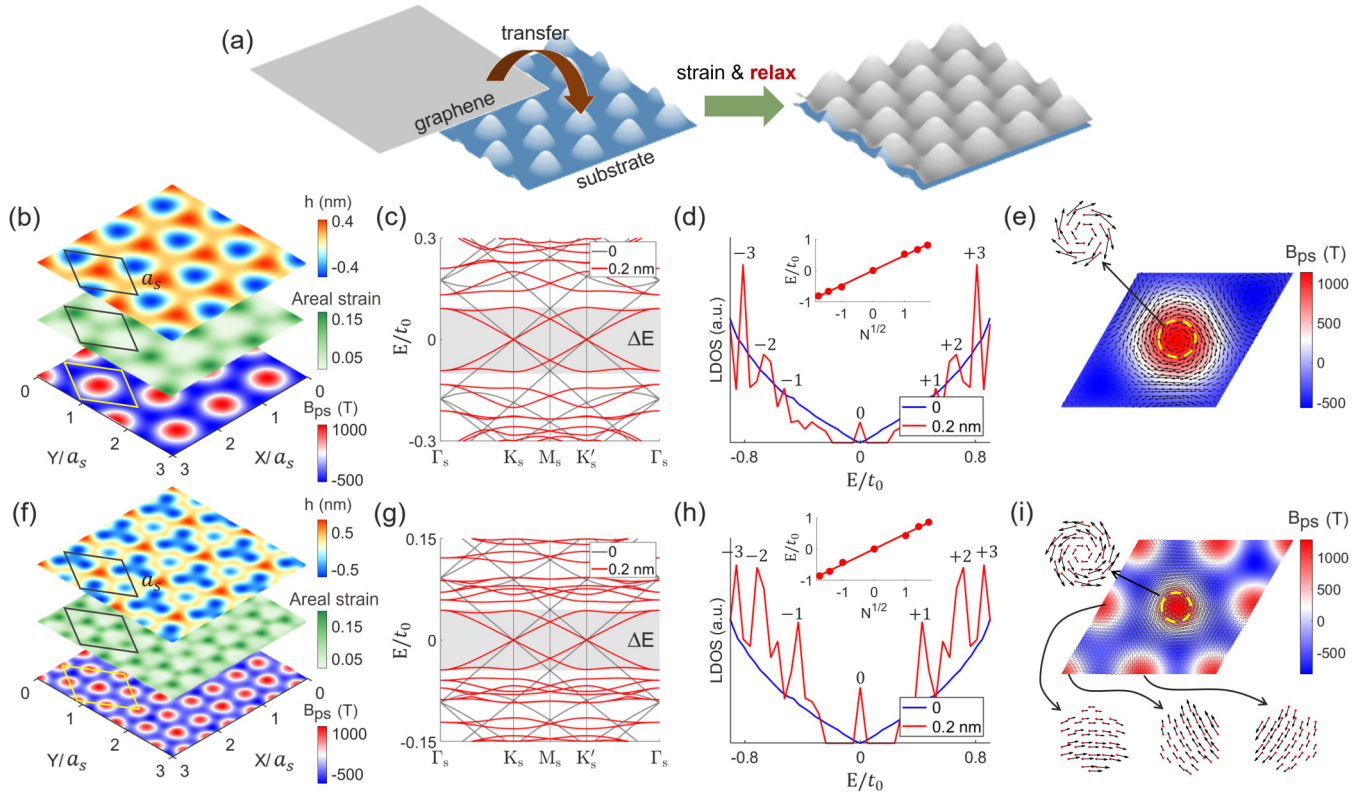


FIG. 1. (a) Schematic of monolayer graphene conforming to substrate topography with strain relaxation. (b)–(e) Results for substrate 1, where superlattice constant $a_s = 20a_0 \approx 4.9$ nm (a_0 is the graphene lattice constant). The height parameter (h_0) is 0.2 nm and the phase (θ) is $\pi/4$. (f)–(i) Results for substrate 2, where $a_s = 40a_0 \approx 9.8$ nm. The height parameter (h_0) is 0.2 nm and phases (θ_a, θ_b) are both $\pi/4$. (b), (f) Out-of-plane deflection (h), areal strain, and pseudomagnetic field (B_{ps}). (c), (g) Band structure for unstrained ($h_0 = 0$, gray curve) and strained ($h_0 = 0.2$ nm, red curve) graphene. The flat band region near Fermi level is shaded in gray, the width of which is denoted as ΔE . (d), (h) LDOS for the central region of the unit cell [circled area in (e) and (i)] for unstrained ($h_0 = 0$, blue curve) and strained ($h_0 = 0.2$ nm, red curve) graphene. Insets show the scaling of pseudo-Landau levels for the strained graphene. (e), (i) Map of interatomic currents, marked by black arrows, within superlattice unit cell for the energy at the edge of shaded flat band [$E/t_0 \approx -0.1$ in (c) and $E/t_0 \approx -0.04$ in (g)] at the \mathbf{K}_s point.

designs in which the flat bands of monolayer graphene can be realized and tuned.

Our study is focused on relaxed monolayer graphene conforming to substrate topography featuring superlattices [Fig. 1(a)]. Due to strain relaxation, the conformation to substrate topography not only imposes the out-of-plane deformations, but also generates in-plane atomistic displacements. Analysis on several representative substrate topographies reveals that substrate-dependent strain relaxation strongly affects flat band structures and associated pseudomagnetic fields. Our approaches are based on continuum theory of elasticity, which requires a suitable model length scale so that the continuum treatment is reasonable [31], and tight-binding assumptions. It is reported that substrate interaction can then be ignored given the model length scale [30,31] so that the substrate is not explicitly modeled by assuming that the graphene membrane completely conforms to the substrate [31]. Also, the tight-binding calculation is based on nearest-neighbor hopping using π electrons. While first-principles calculations can produce more accurate results, they can be computationally prohibitive given the model length scales. Our analytical approach can access larger model length scales (i.e., larger substrate height modulation and superlattice periodicity) for theoretical guidance.

II. TOPOGRAPHY-DEPENDENT FLAT BANDS AND GIANT PSEUDOMAGNETIC FIELDS

The first substrate topography (substrate 1) is

$$h = h_0 \sum_{i=1}^3 \cos(\mathbf{G}_i \cdot \mathbf{r} + \theta_i). \quad (1)$$

The second substrate topography (substrate 2) is

$$h = h_0 \left[\sum_{i=1}^3 \cos(\mathbf{G}_i \cdot \mathbf{r} + \theta'_i) + \sum_{i=1}^3 \cos(2\mathbf{G}_i \cdot \mathbf{r} + \theta''_i) \right]. \quad (2)$$

Substrate 1 [Figs. 1(b)–1(e)] represents a typical periodic system that generates flat bands in monolayer graphene [2,16–18], while substrate 2 [Figs. 1(f)–1(i)] results from additional periodic perturbations that would produce additional relaxation behaviors. The results for substrate 3, which captures the gradual transition from substrate 1 to substrate 2, and the results for substrate 4, featuring square superlattice, can be found in the Supplemental Material (SM) [32].

In the above expressions, $\mathbf{G}_1 = \frac{2\pi}{a_s}(0, \frac{2}{\sqrt{3}})$, $\mathbf{G}_2 = \frac{2\pi}{a_s}(-1, -\frac{1}{\sqrt{3}})$, and $\mathbf{G}_3 = -(\mathbf{G}_1 + \mathbf{G}_2)$ are reciprocal lattice vectors of the graphene superlattice unit cell with side length a_s

[Figs. 1(b) and 1(f)]. Note that a_s should be an integer multiple of the graphene lattice constant ($a_0 = \sqrt{3}a_{CC}$, where a_{CC} is the carbon-carbon bond length) in real space. The θ_i , θ_i' , θ_i'' are three tunable phase angles.

In continuum mechanics, the elastic energy of the graphene membrane in a superlattice unit cell can be calculated as

$$E_{\text{clas}} = \frac{Et}{2(1-v^2)} \int [u_{xx}^2 + u_{yy}^2 + 2vu_{xx}u_{yy} + 2(1-v)u_{xy}^2] d^2r, \quad (3)$$

where graphene is modeled [33–35] with Young's modulus (E) of 1 TPa, Poisson's ratio (v) of 0.17, and thickness (t) of 0.34 nm.

The strain tensor is computed as

$$u_{ij} = \frac{1}{2} \left(\frac{\partial u_i}{\partial j} + \frac{\partial u_j}{\partial i} \right) + \frac{1}{2} \left(\frac{\partial h}{\partial i} \frac{\partial h}{\partial j} \right), \quad (4)$$

where $\{i, j\} = \{x, y\}$.

The analytical expressions for periodic in-plane displacements are obtained by extremizing the elastic energy function [31] (see more details in the SM [32]).

The in-plane displacements for substrate 1 are derived as

$$\begin{aligned} u_x = & \frac{h_0^2 \pi}{4a_s} [-\sin(2\mathbf{G}_2 \cdot \mathbf{r} + 2\theta) + \sin(2\mathbf{G}_3 \cdot \mathbf{r} + 2\theta)] \\ & + \frac{h_0^2 \pi(-1+3v)}{4a_s} [\sin(\mathbf{G}_2 \cdot \mathbf{r} - 2\theta) - \sin(\mathbf{G}_3 \cdot \mathbf{r} - 2\theta)] \\ & + \frac{h_0^2 \pi(3-v)}{12a_s} [\sin((\mathbf{G}_1 - \mathbf{G}_2) \cdot \mathbf{r}) \\ & - \sin((\mathbf{G}_1 - \mathbf{G}_3) \cdot \mathbf{r}) - 2\sin((\mathbf{G}_2 - \mathbf{G}_3) \cdot \mathbf{r})], \end{aligned} \quad (5)$$

$$\begin{aligned} u_y = & \frac{h_0^2 \pi}{4\sqrt{3}a_s} [2\sin(2\mathbf{G}_1 \cdot \mathbf{r} + 2\theta) - \sin(2\mathbf{G}_2 \cdot \mathbf{r} + 2\theta) \\ & - \sin(2\mathbf{G}_3 \cdot \mathbf{r} + 2\theta)] \\ & + \frac{h_0^2 \pi(-1+3v)}{4\sqrt{3}a_s} [-2\sin(\mathbf{G}_1 \cdot \mathbf{r} - 2\theta) \\ & + \sin(\mathbf{G}_2 \cdot \mathbf{r} - 2\theta) + \sin(\mathbf{G}_3 \cdot \mathbf{r} - 2\theta)] \\ & + \frac{h_0^2 \pi(3-v)}{4\sqrt{3}a_s} [\sin((\mathbf{G}_1 - \mathbf{G}_2) \cdot \mathbf{r}) + \sin((\mathbf{G}_1 - \mathbf{G}_3) \cdot \mathbf{r})]. \end{aligned} \quad (6)$$

The associated pseudomagnetic field for substrate 1 is then

$$B_{\text{ps}} = -\frac{6t_0\beta h_0^2 \pi^3(1+v)}{\sqrt{3}ev_F a_s^3} \sum_{i=1}^3 \sin(\mathbf{G}_i \cdot \mathbf{r} - 2\theta). \quad (7)$$

In the above equations, $\theta = (\theta_1 + \theta_2 + \theta_3)/3$, t_0 is the equilibrium hopping energy between nearest carbon atoms in graphene, β is a dimensionless constant, e is the elementary charge, and v_F ($= \frac{3t_0 a_{CC}}{2\hbar}$) is the Fermi velocity. These parameters originate from the Dirac Hamiltonian of graphene [16,21,24,26,36] and the bond-strain dependent hopping energies (t_{ij}), which can be described as

$$t_{ij} = t_0 e^{-\beta(\frac{r_{ij}}{a_{cc}} - 1)}, \quad (8)$$

where $a_{cc} = 0.142$ nm is the equilibrium bond length in graphene, and $r_{ij} = |\mathbf{r}_i - \mathbf{r}_j|$ is the length of the strained bond between atoms i and j . We use $t_0 = 2.7$ eV, $\beta = 3.37$ in our calculations.

The pseudomagnetic field for substrate 2 is

$$\begin{aligned} B_{\text{ps}} = & -\frac{6t_0\beta h_0^2 \pi^3(1+v)}{\sqrt{3}ev_F a_s^3} \sum_{i=1}^3 \sin(\mathbf{G}_i \cdot \mathbf{r} - 2\theta_a) \\ & - \frac{48t_0\beta h_0^2 \pi^3(1+v)}{\sqrt{3}ev_F a_s^3} \sum_{i=1}^3 \sin(2\mathbf{G}_i \cdot \mathbf{r} - 2\theta_b) \\ & - \frac{240t_0\beta h_0^2 \pi^3(1+v)}{49\sqrt{3}ev_F a_s^3} [\sin((2\mathbf{G}_1 - \mathbf{G}_3) \cdot \mathbf{r} - (\theta_a - \theta_b)) \\ & + \sin((2\mathbf{G}_1 - \mathbf{G}_2) \cdot \mathbf{r} - (\theta_a - \theta_b)) \\ & + \sin((2\mathbf{G}_2 - \mathbf{G}_3) \cdot \mathbf{r} - (\theta_a - \theta_b)) \\ & + \sin((2\mathbf{G}_3 - \mathbf{G}_2) \cdot \mathbf{r} - (\theta_a - \theta_b)) \\ & + \sin((2\mathbf{G}_2 - \mathbf{G}_1) \cdot \mathbf{r} - (\theta_a - \theta_b)) \\ & + \sin((2\mathbf{G}_3 - \mathbf{G}_1) \cdot \mathbf{r} - (\theta_a - \theta_b))], \end{aligned} \quad (9)$$

where $\theta_a = (\theta_1' + \theta_2' + \theta_3')/3$, $\theta_b = (\theta_1'' + \theta_2'' + \theta_3'')/3$, while the analytical expressions for in-plane displacements are documented in the SM [32].

The above analytical expressions serve as foundations for the subsequent quantum mechanical calculations on electronic band structures. Figures 1(b) and 1(f) show the height profile, areal strain ($=u_{xx} + u_{yy} + u_{xx}u_{yy}$) and the resultant pseudomagnetic field after relaxation using representative examples for substrate 1 and 2, respectively. In an example for substrate 1 [Fig. 1(b)], $a_s = 20a_0 \approx 4.9$ nm, $h_0 = 0.2$ nm, and $\theta = \pi/4$. In an example for substrate 2 [Fig. 1(f)], $a_s = 40a_0 \approx 9.8$ nm, $h_0 = 0.2$ nm, and $\theta_a = \theta_b = \pi/4$. The detailed morphologies of the substrate height profile and the distribution of strain components are found in Fig. S1 of the SM [32].

For substrate 1, the pseudomagnetic field distribution resembles those found in experimental and theoretical studies for buckled monolayer graphene [2,16–18]. The isolated quasiuniform circular field regions, whose intensity reaches 1000 T, are embedded in field regions with opposite signs with intensity reaching 500 T [Fig. 1(b)]. These isolated quasiuniform field regions are arranged in a triangular lattice. The maximum areal strain reaches about 0.16, corresponding to the maximum strain (i.e., u_{xx} or u_{yy}) about 0.08, which is a reasonable strain where graphene is treated as linear elastic. It is also interesting to see that the isolated quasiuniform circular field regions are not correlated with the region with the maximum areal strain, but with areal strain of about 0.09 (at the center of the superlattice unit cell) which also has the maximum height. Compared with substrate 1, the topography of substrate 2 has an additional perturbation term, leading to drastic differences in the distribution of areal strain and pseudomagnetic fields. As shown later, the superlattice unit cell as shown for substrate 2 contains many isolated quasiuniform field regions arranged in a similar triangular lattice. Nevertheless, for both substrates, the isolated regions correspond to locations with relatively small areal strain.

We use the nearest-neighbor tight-binding model on the relaxed configuration given by

$$H = \sum_{i,j} t_{ij} c_i^\dagger c_j, \quad (10)$$

where c_i^\dagger (c_i) is the creation (annihilation) operator for an electron at site i , and the bond-strain dependent hopping energies (t_{ij}) are calculated by the derived analytical displacements.

Figures 1(c) and 1(g) are the calculated band structures for two substrates. The band structures of undeformed flat pristine graphene are used for contrast. Flat bands emerge near the Fermi level (marked by shading area) with similar energy dispersion relationship for both substrates. Other flat bands away from Fermi level are also visible. This is attributed to the periodic pseudomagnetic field that is strong enough to influence the motion of electrons and generate band gaps. Nevertheless, the distinct features in energy dispersion in other flat bands suggest that the electron dynamics are strongly dependent on designs of substrate topographies.

To quantify and validate the strong pseudomagnetic fields, we calculate the local density of states [LDOS, in Figs. 1(d) and 1(h)] for isolated quasiuniform field regions [the circled areas in Figs. 1(e) and 1(i)] at the center of the superlattice unit cell in order to identify the pseudo-Landau levels (pLLs) originating from pseudomagnetic fields [21,22]. The LDOS for the flat pristine graphene is to highlight the emergence of pLLs. Specifically, the energy peaks of pLLs should follow the linear scaling with respect to the square root of quantum number labeling the pLLs [21,22],

$$E_n = \text{sgn}(n) v_F \sqrt{2e\hbar B |n|}. \quad (11)$$

From our tight-binding calculations for both substrates, the quantum numbers labeling the pLLs can be feasibly identified and the linear scaling relationships can be satisfied [insets in Figs. 1(d) and 1(h)], which correspond to pseudomagnetic field intensities of about 1000 and 1100 T, consistent with the analytical derivation as shown in Figs. 1(e) and 1(i), respectively. Such giant intensities are promising given experimental evidence of giant pseudomagnetic fields near 1000 T in strained monolayer graphene [28,37]. The maximum strain after relaxation in our study does not exceed 10%, which is experimentally feasible given that tensile strains ranging 1.32–25% have been proposed in a variety of experimental settings [37–39]. Figure S2 of the SM shows the evolution of pLLs as the substrate topography changes [32], as well as the appearance of double peak at zeroth pLL that is consistent with computational findings on periodically buckled monolayer graphene [2].

Although the isolated quasiuniform pseudomagnetic fields are arranged in triangular lattices for both substrate topographies, they have different influences on the electronic states at the flat bands. For demonstration, we calculate the interatomic currents for the energy at the edge of the flat band ($E/t_0 \approx \pm 0.1$ for substrate 1 and $E/t_0 \approx \pm 0.04$ for substrate 2) on several representative points in reciprocal space.

The current is calculated using

$$\mathbf{J}_{\mathbf{k},i}(E) = \frac{4e}{h} \sum_{j=1}^3 \text{Im}(\Psi_{\mathbf{k},i}(E) |H_{ij}| \Psi_{\mathbf{k},j}(E)) \mathbf{e}_{ij}, \quad (12)$$

where $\mathbf{J}_{\mathbf{k},i}(E)$ is the current vector at atom i calculated as a sum of currents flowing between atom i and its three nearest neighbors at energy E due to an electron in state \mathbf{k} , \hbar is the Planck constant, $|\Psi_{\mathbf{k},i}\rangle$ is the wave function of the \mathbf{k} state at atom i , H_{ij} is the Hamiltonian matrix element between atoms i and j , and \mathbf{e}_{ij} is the unit vector in the direction of the bond between atoms i and j .

Figure 1(e) shows that for substrate 1, most of the electrons at the flat band energy ($E/t_0 \approx -0.1$) at the \mathbf{K}_s point perform closed-loop circular motion (clockwise) with radius of atomic scale under the influence of the isolated quasiuniform pseudomagnetic field. This provides an intuitive illustration of the strong confinement effect from the strong pseudomagnetic field reaching 1000 T. Nevertheless, Fig. 1(i) shows that for substrate 2, only the isolated quasiuniform field region, which corresponds to the largest out-of-plane deformation (at the central region of the superlattice unit cell with intensity about 1100 T), is the vortex center of the counterclockwise atomic currents at the flat band energy ($E/t_0 \approx -0.04$) at the \mathbf{K}_s point. At other isolated quasiuniform field regions (at the edge of superlattice unit cell with weaker intensity about 1000 T), the atomic currents pass through and turn in a clockwise direction [Fig. 1(i)]. The circular-motion interatomic current may appear at other electronic states (Fig. S3 [32]), while being affected by the negative field. The calculations in substrate 3 where the gradual transition from substrate 1 to substrate 2 can be programmed show similar conclusions (Fig. S4 [32]). The above discussions show that different substrate topographies can lead to a diverse mechanism of electron confinement that gives rise to the band flattening, although the distributions of pseudomagnetic fields can be similar. Note that the pseudomagnetic fields in the current work originate from static strain gradient field [2,21,22,24]. The pseudoelectric field due to dynamic strain gradient [40,41] is beyond the scope of the current work. The pseudomagnetic fields in the current work in combination with scalar fields [42] due to the strain gradient can also be used to explore valley scattering behaviors [43].

III. EFFECT OF TOPOGRAPHY-DEPENDENT STRAIN RELAXATION

A particular focus of this work is to quantify the effect of strain relaxation on producing strong pseudomagnetic fields and flat bands. In a recent study [30], the in-plane relaxation is discussed using an indeterminate dimensionless fitting parameter, which reports that the strain relaxations for a few substrates serve as higher order corrections. Nevertheless, our current work, based on analytical displacement fields due to relaxation, shows that the effects of strain relaxation on flat bands highly depend on substrate topography, and can be very strong. The comparisons are made with unrelaxed models whose atoms only have out-of-plane displacements to fit the substrate topography. Without strain relaxation, the in-plane atomistic displacements are zero so that all the in-plane strain components as well as pseudomagnetic fields are completely determined by the out-of-plane displacements. The analytical expressions for pseudomagnetic fields for unrelaxed models are listed in the SM [32]. For both substrate topographies, we consider the situations where u_{xx} and u_{yy} after relaxation do not exceed 0.1 and phases (θ or θ_a and θ_b) remain $\pi/4$.

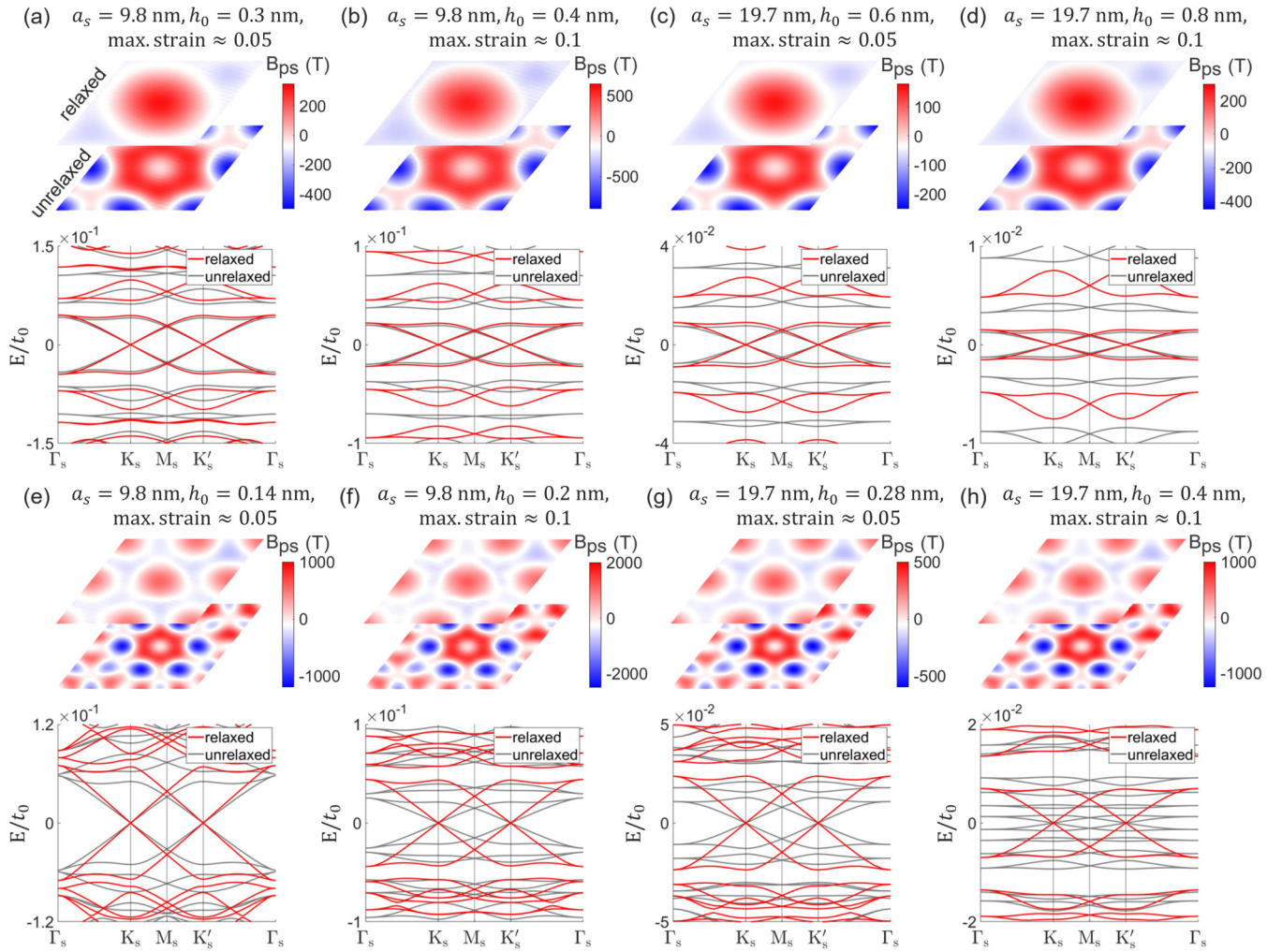


FIG. 2. Pseudomagnetic fields and band structures of relaxed and unrelaxed graphene conforming to substrate topography. Phases (θ or θ_a and θ_b) are uniformly $\pi/4$. Each panel is labeled with corresponding superlattice constant (a_s), height parameters (h_0), and maximum strain in u_{xx} or u_{yy} . (a)–(d) Results for substrate 1, showing that relaxation induces larger energy gaps. (e)–(h) Results for substrate 2, showing that relaxation strongly modifies band structures.

The complete geometric parameters describing a series of substrate topographies are labeled in each panel of Fig. 2. See Figs. S5 and S6 for a smaller strain regime and the connection to the maximum curvature of topography [32]. Contrasting among these results reveals a topography-dependent relaxation effect.

Figures 2(a)–2(d) show the effect of relaxation on pseudomagnetic fields as well as flat band structures using four models of substrate 1. Each model can be characterized by the maximum strain after relaxation and the geometric spacing between the periodic modulations (i.e., the superlattice constant a_s) on substrate 1. For all unrelaxed models, the field region at the center of the superlattice unit cell carries a hexagon shape. The field intensities at the central region reduce to zero because without strain relaxation the strain gradients in the central region vanish. In addition, the intensity of the field with opposite sign is much stronger compared with that of the relaxed case. For the same superlattice constant a_s [comparing Fig. 2(a) with 2(b), or Fig 2(c) with 2(d)], larger maximum strain increases the overall field intensities. For the same maximum strain [comparing Fig. 2(a) with

2(c), or Fig. 2(b) with 2(d)], larger superlattice constant a_s reduces the overall field intensities. More insight regarding the effect of relaxation can be read from band structures. We find that for models of substrate 1, the strain relaxation has limited influence on the flat band near the Fermi level. Nevertheless, other flat bands away from the Fermi level begin to exhibit considerable differences in terms of energy values and the width of bands. Particularly, for the same superlattice constant a_s [comparing Fig. 2(a) with 2(b), or Fig. 2(c) with 2(d)], the relaxation increases the energy gap between the flat band near the Fermi level and the next flat band. For the same maximum strain [comparing Fig. 2(a) with 2(c), or Fig. 2(b) with 2(d)], the larger superlattice constant a_s enhances the relaxation-induced discrepancies in flat energy bands away from the Fermi level. For example, in Fig. 2(d), except for the flat band near Fermi level, the other flat bands as shown for relaxed and unrelaxed models have no overlap in energy. For substrate 1, relaxation induces larger energy gaps.

Nevertheless, more a pronounced effect from relaxation is found for the case of substrate 2, as shown in Figs. 2(e)–2(h)

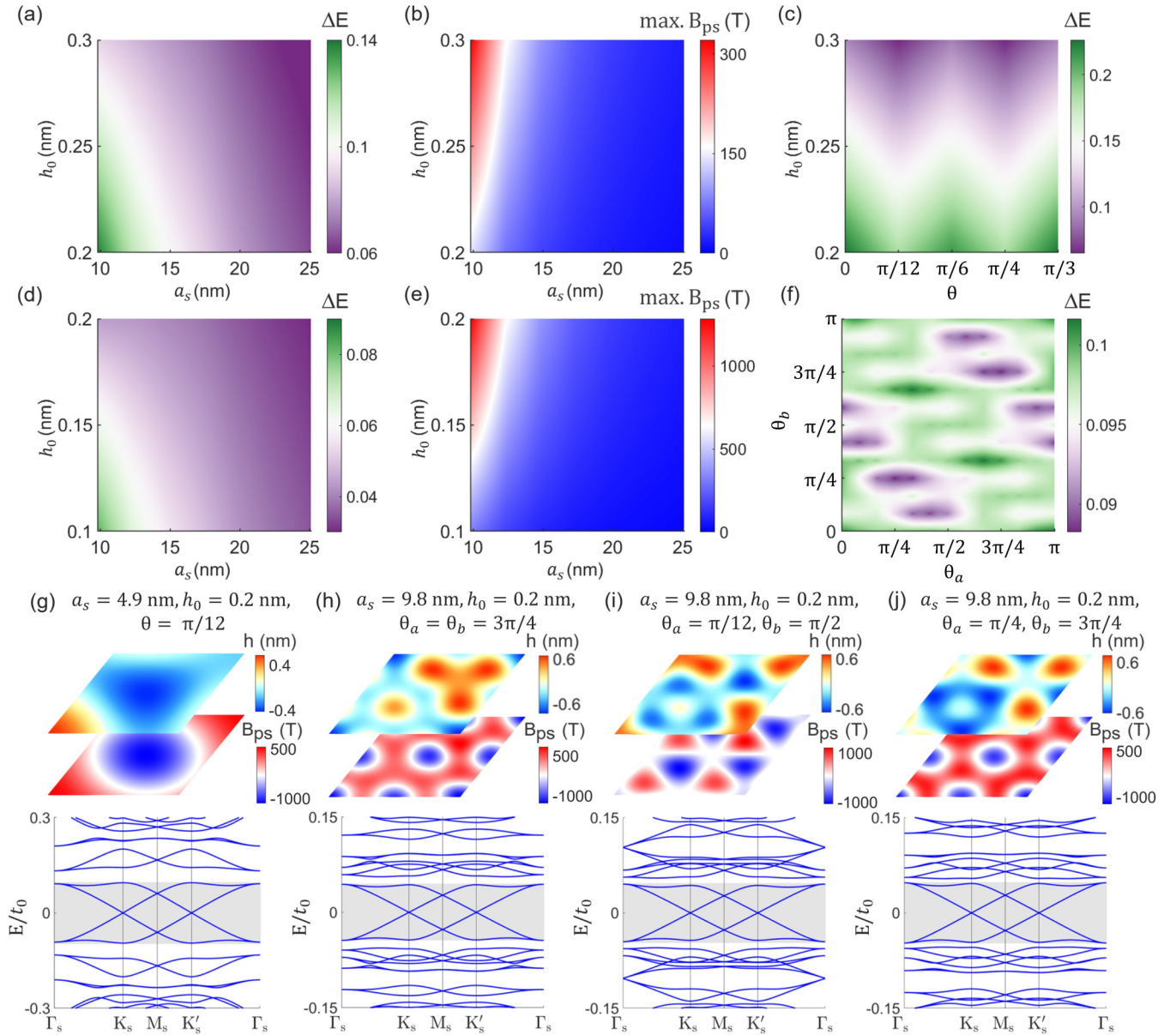


FIG. 3. (a)–(f) Map of the width (ΔE) of flat band near Fermi level and the maximum pseudomagnetic field intensity ($\max. B_{ps}$) in the space of superlattice constant (a_s), height parameter (h_0), and phases (θ , θ_a , θ_b). (a)–(c) Results for substrate 1. The phase θ in (a) and (b) is $\pi/4$. The superlattice constant (a_s) in (c) is 4.9 nm. (d)–(f) Results for substrate 2. The phases θ_a and θ_b in (d) and (e) are $\pi/4$. The superlattice constant (a_s) and the height parameter (h_0) in (f) are 9.8 and 0.2 nm, respectively. (g)–(j) Out-of-plane deflection (h), pseudomagnetic field (B_{ps}), and flat band structures of different substrate designs. Each column is labeled with superlattice constant (a_s), height parameters (h_0), and phases. (g) Result for substrate 1. (h)–(j) Results for substrate 2.

again using four models from combinations of two maximum strains after relaxation and two superlattice constants. In terms of the pseudomagnetic field, the unrelaxed model gives rise to a much more complicated distribution pattern as compared with the relaxed model, whose isolated quasiuniform field regions are arranged in a triangular lattice. While the effect of relaxation on intensities of pseudomagnetic fields are similar as in the preceding discussion of substrate 1, the strain relaxation for substrate 2 has strong influence on all flat bands, in sharp contrast with the observation for substrate 1. The discrepancies in energy dispersion of flat bands as well as the gaps between flat bands are significantly dependent on strain

relaxation for substrate 2. Particularly, for the same superlattice constant a_s [comparing Fig. 2(e) with 2(f), or Fig. 2(g) with 2(h)], the relaxation strongly affects the energy dispersion of the first flat band near the Fermi level, and increases the energy gap between the flat bands. For the same maximum strain [comparing Fig. 2(e) with 2(g), or Fig. 2(f) with 2(h)], the larger superlattice constant (a_s) enhances the relaxation-induced discrepancies in flat bands. For example, in Fig. 2(h), the energy range of the single flat band near the Fermi level for the relaxed model almost covers five neighboring flat bands for the unrelaxed model. For substrate 2, the band structures are strongly modified by strain relaxation. Similar conclusions

are found for substrate 3 (Fig. S4) highlighting the transition between substrate 1 and substrate 2 [32].

The above discussion shows that not knowing or neglecting the structural relaxation can lead to significant errors. While for certain topography (e.g., substrate 1) the flat band near the Fermi level is not sensitive to strain relaxation, relaxation can induce larger energy gaps between flat bands. For other types of topography (e.g., substrates 2 and 3), the strain relaxation strongly affects the flat band near the Fermi level.

IV. DESIGNING FLAT BANDS AND STRONG PSEUDOMAGNETIC FIELDS BY TOPOGRAPHY

Our preceding analysis shows that the strong pseudomagnetic fields as well as flat bands of monolayer graphene are highly sensitive to substrate-dependent strain relaxation, which may not be simply neglected. With the analytical expressions of relaxed atomistic displacements coupled to substrate topography, large-scale quantum mechanical calculations respecting the effect of relaxation can be carried out for rational design on electronic properties. For demonstration, we reveal diagrams correlating the geometric parameters of substrate topography to the flat band structure and pseudomagnetic field. We show a variety of flat band structures that can be realized by relaxing on topography of substrate 1 [Figs. 3(a)–3(c)], substrate 2 [Figs. 3(d)–3(f)], and substrate 3 (Fig. S4), along with several particular examples [Figs. 3(g)–3(j), Figs. S7–S13 [32]]. The variation of phases can lead to diverse geometries.

Figures 3(a) and 3(b) present effects of the superlattice constant (a_s) and the height parameter (h_0) on the flat band width (ΔE) near the Fermi level (as illustrated in Fig. 1) and the maximum pseudomagnetic intensity for substrate 1. The smaller the ΔE , the stronger the kinetic energy of electrons is quenched near the Fermi level. The phase (θ) is uniformly $\pi/4$. At the same superlattice constant (a_s), the larger the height parameter (h_0), the smaller the flat band width (ΔE) and the higher the maximum field intensity (max. B_{ps}). On the other hand, at the same height parameter (h_0), the larger the superlattice constant (a_s), the smaller the flat band width (ΔE), and the smaller the maximum field intensity (max. B_{ps}). Figure 3(c) illustrates effects of the phase (θ) and the height parameter (h_0) on the flat band width (ΔE) when the superlattice constant (a_s) is 4.9 nm. When θ changes from 0 to $\pi/6$ and from $\pi/6$ to $\pi/3$, the flat band width (ΔE) first decreases and then increases. Local minima are located at $\pi/12$ and $\pi/4$. Figure 3(g) plots the substrate topography and pseudomagnetic field when the phase (θ) is $\pi/12$. Compared with the case where the phase (θ) is $\pi/4$ (e.g., see Figs. 1 and 2), the central field intensity changes the sign and the band structure features are totally consistent.

Figures 3(d) and 3(e) present effects of superlattice constant (a_s) and the height parameter (h_0) on the flat band width (ΔE) and the maximum pseudomagnetic field intensity (max. B_{ps}) for substrate 2, where the phases (θ_a , θ_b) are uniformly $\pi/4$. Both diagrams are visually consistent with the case of substrate 1. Nevertheless, Fig. 3(f) renders the diagram of the flat band width (ΔE) under different combinations of θ_a and θ_b , where the superlattice constant (a_s) and the height parameter (h_0) are kept at 9.8 and 0.2 nm, respectively. The pseudomagnetic fields and flat band structures from three combinations of θ_a and θ_b , corresponding to local minimum of the flat band width (ΔE), are shown in Figs. 3(h) and 3(j). The pseudomagnetic fields in Fig. 3(h) and 3(j) both possess isolated circular quasiuniform field regions, while the pseudomagnetic field in Fig. 3(i) has triangular quasiuniform field regions with alternative signs. These results demonstrate rich designing opportunities towards flat bands from monolayer graphene.

Our theoretical approach can be used to explore other periodic topography as well. For example, we find that for substrate featuring square superlattices (Fig. S14 [32]), relaxation-dependent band flattening is observed in particular regions in the Brillouin zone.

V. CONCLUSIONS

With topography-dependent strain relaxation fully considered, large-scale tight-binding calculations based on analytical displacement fields are carried out to achieve rational design on flat band structures and strong pseudomagnetic fields in monolayer graphene. We find that quantitatively the flat band structures as well as strong pseudomagnetic fields are highly sensitive to strain relaxation and substrate topography. A collection of topography designs to realize flat bands in monolayer graphene is proposed. Our study contributes to the understanding of flat band structures and strong pseudomagnetic fields in monolayer graphene via topography strain engineering.

ACKNOWLEDGMENTS

This work was supported by National Key R&D Program of China (Grant No. 2023YFC2812700), the National Natural Science Foundation of China (Grants No. 12272337 and No. 12002304), the Distinguished Young Scientists Fund from the Natural Science Foundation of Zhejiang Province (Grant No. LR23A020001), Laoshan Laboratory (Grant No. LSKJ202205300), and the ‘‘Pioneer’’ R&D Program of Zhejiang (Grant No. 2023C03007). The authors also acknowledge funding support from Zhejiang University.

There are no conflicts of interest.

[1] R. Bistritzer and A. H. MacDonald, Moiré bands in twisted double-layer graphene, *Proc. Natl. Acad. Sci. USA* **108**, 12233 (2011).

[2] J. Mao *et al.*, Evidence of flat bands and correlated states in buckled graphene superlattices, *Nature (London)* **584**, 215 (2020).

- [3] Y. Cao, V. Fatemi, S. Fang, K. Watanabe, T. Taniguchi, E. Kaxiras, and P. Jarillo-Herrero, Unconventional superconductivity in magic-angle graphene superlattices, *Nature (London)* **556**, 43 (2018).
- [4] G. Chen *et al.*, Signatures of tunable superconductivity in a trilayer graphene moiré superlattice, *Nature (London)* **572**, 215 (2019).
- [5] J. M. Park, Y. Cao, K. Watanabe, T. Taniguchi, and P. Jarillo-Herrero, Tunable strongly coupled superconductivity in magic-angle twisted trilayer graphene, *Nature (London)* **590**, 249 (2021).
- [6] N. B. Kopnin, M. Ijäs, A. Harju, and T. T. Heikkilä, High-temperature surface superconductivity in rhombohedral graphite, *Phys. Rev. B* **87**, 140503(R) (2013).
- [7] N. B. Kopnin, T. T. Heikkilä, and G. E. Volovik, High-temperature surface superconductivity in topological flat-band systems, *Phys. Rev. B* **83**, 220503(R) (2011).
- [8] Z. Bi, N. F. Q. Yuan, and L. Fu, Designing flat bands by strain, *Phys. Rev. B* **100**, 035448 (2019).
- [9] Y. Choi *et al.*, Electronic correlations in twisted bilayer graphene near the magic angle, *Nat. Phys.* **15**, 1174 (2019).
- [10] Y. Xie, B. Lian, B. Jäck, X. Liu, C.-L. Chiu, K. Watanabe, T. Taniguchi, B. A. Bernevig, and A. Yazdani, Spectroscopic signatures of many-body correlations in magic-angle twisted bilayer graphene, *Nature (London)* **572**, 101 (2019).
- [11] N. N. T. Nam and M. Koshino, Lattice relaxation and energy band modulation in twisted bilayer graphene, *Phys. Rev. B* **96**, 075311 (2017).
- [12] H. Yoo *et al.*, Atomic and electronic reconstruction at the van der waals interface in twisted bilayer graphene, *Nat. Mater.* **18**, 448 (2019).
- [13] F. Mesple, A. Missaoui, T. Cea, L. Huder, F. Guinea, G. Trambly De Laissardière, C. Chapelier, and V. T. Renard, Heterostrain determines flat bands in magic-angle twisted graphene layers, *Phys. Rev. Lett.* **127**, 126405 (2021).
- [14] G. Tarnopolsky, A. J. Kruchkov, and A. Vishwanath, Origin of magic angles in twisted bilayer graphene, *Phys. Rev. Lett.* **122**, 106405 (2019).
- [15] A. Uri *et al.*, Mapping the twist-angle disorder and landau levels in magic-angle graphene, *Nature (London)* **581**, 47 (2020).
- [16] S. P. Milovanović, M. Anđelković, L. Covaci, and F. M. Peeters, Band flattening in buckled monolayer graphene, *Phys. Rev. B* **102**, 245427 (2020).
- [17] A. L. R. Manesco, J. L. Lado, E. V. S. Ribeiro, G. Weber, and D. Rodrigues, Jr., Correlations in the elastic landau level of spontaneously buckled graphene, *2D Mater.* **8**, 015011 (2021).
- [18] A. L. R. Manesco and J. L. Lado, Correlation-induced valley topology in buckled graphene superlattices, *2D Mater.* **8**, 035057 (2021).
- [19] Q. Gao, J. Dong, P. Ledwith, D. Parker, and E. Khalaf, Untwisting moiré physics: Almost ideal bands and fractional chern insulators in periodically strained monolayer graphene, *Phys. Rev. Lett.* **131**, 096401 (2023).
- [20] V. T. Phong and E. J. Mele, Boundary modes from periodic magnetic and pseudomagnetic fields in graphene, *Phys. Rev. Lett.* **128**, 176406 (2022).
- [21] F. Guinea, M. I. Katsnelson, and A. K. Geim, Energy gaps and a zero-field quantum Hall effect in graphene by strain engineering, *Nat. Phys.* **6**, 30 (2010).
- [22] N. Levy, S. A. Burke, K. L. Meaker, M. Panlasigui, A. Zettl, F. Guinea, A. H. C. Neto, and M. F. Crommie, Strain-induced pseudo-magnetic fields greater than 300 Tesla in graphene nanobubbles, *Science* **329**, 544 (2010).
- [23] S. Zhu, Y. Huang, N. N. Klimov, D. B. Newell, N. B. Zhitenev, J. A. Stroscio, S. D. Solares, and T. Li, Pseudomagnetic fields in a locally strained graphene drumhead, *Phys. Rev. B* **90**, 075426 (2014).
- [24] S. Zhu, J. A. Stroscio, and T. Li, Programmable extreme pseudomagnetic fields in graphene by a uniaxial stretch, *Phys. Rev. Lett.* **115**, 245501 (2015).
- [25] P. Jia *et al.*, Programmable graphene nanobubbles with three-fold symmetric pseudo-magnetic fields, *Nat. Commun.* **10**, 3127 (2019).
- [26] N. N. Klimov, S. Jung, S. Zhu, T. Li, C. A. Wright, S. D. Solares, D. B. Newell, N. B. Zhitenev, and J. A. Stroscio, Electromechanical properties of graphene drumheads, *Science* **336**, 1557 (2012).
- [27] G. G. Naumis, S. A. Herrera, S. P. Poudel, H. Nakamura, and S. Barraza-Lopez, Mechanical, electronic, optical, piezoelectric and ferroic properties of strained graphene and other strained monolayers and multilayers: An update, *Rep. Prog. Phys.* **87**, 016502 (2024).
- [28] A. Georgi *et al.*, Tuning the pseudospin polarization of graphene by a pseudomagnetic field, *Nano Lett.* **17**, 2240 (2017).
- [29] G. J. Verbiest, S. Brinker, and C. Stampfer, Uniformity of the pseudomagnetic field in strained Graphene, *Phys. Rev. B* **92**, 075417 (2015).
- [30] M. T. Mahmud, D. Zhai, and N. Sandler, Topological flat bands in strained graphene: substrate engineering and optical control, *Nano Lett.* **23**, 7725 (2023).
- [31] F. Guinea, B. Horovitz, and P. Le Doussal, Gauge field induced by ripples in graphene, *Phys. Rev. B* **77**, 205421 (2008).
- [32] See Supplemental Material at <http://link.aps.org/supplemental/10.1103/PhysRevB.109.245408> for more details on theoretical framework, analytical results, and tight-binding results.
- [33] E. Muñoz, A. K. Singh, M. A. Ribas, E. S. Penev, and B. I. Yakobson, The ultimate diamond slab: Graphane versus graphene, *Diamond Relat. Mater.* **19**, 368 (2010).
- [34] Q. X. Pei, Y. W. Zhang, and V. B. Shenoy, A molecular dynamics study of the mechanical properties of hydrogen functionalized graphene, *Carbon* **48**, 898 (2010).
- [35] E. Cadelano, P. L. Palla, S. Giordano, and L. Colombo, Elastic properties of hydrogenated graphene, *Phys. Rev. B* **82**, 235414 (2010).
- [36] Z. Qi, A. L. Kitt, H. S. Park, V. M. Pereira, D. K. Campbell, and A. H. Castro Neto, Pseudomagnetic fields in graphene nanobubbles of constrained geometry: A molecular dynamics study, *Phys. Rev. B* **90**, 125419 (2014).
- [37] C.-C. Hsu, M. L. Teague, J.-Q. Wang, and N.-C. Yeh, Nanoscale strain engineering of giant pseudo-magnetic fields, valley polarization, and topological channels in graphene, *Sci. Adv.* **6**, eaat9488 (2020).
- [38] D.-H. Kang *et al.*, Pseudo-magnetic field-induced slow carrier dynamics in periodically strained graphene, *Nat. Commun.* **12**, 5087 (2021).
- [39] H. Li *et al.*, Optoelectronic crystal of artificial atoms in strain-textured molybdenum disulphide, *Nat. Commun.* **6**, 7381 (2015).

- [40] E. Sela, Y. Bloch, F. Von Oppen, and M. B. Shalom, Quantum Hall response to time-dependent strain gradients in graphene, *Phys. Rev. Lett.* **124**, 026602 (2020).
- [41] N. Hadadi, A. Belayadi, A. AlRabiah, O. Ly, C. A. Akosa, M. Vogl, H. Bahlouli, A. Manchon, and A. Abbout, Pseudo electric field and pumping valley current in graphene nanobubbles, *Phys. Rev. B* **108**, 195418 (2023).
- [42] H. Suzuura and T. Ando, Phonons and electron-phonon scattering in carbon nanotubes, *Phys. Rev. B* **65**, 235412 (2002).
- [43] R. Carrillo-Bastos, M. Ochoa, S. A. Zavala, and F. Mireles, Enhanced asymmetric valley scattering by scalar fields in nonuniform out-of-plane deformations in graphene, *Phys. Rev. B* **98**, 165436 (2018).